INTERNATIONAL JOURNAL FOR NUMERICAL METHODS IN FLUIDS, VOL. 12, 343–367 (1991)

THE APPLICATION OF FINITE ELEMENT ANALYSIS TO THE SOLUTION OF STOKES WAVE DIFFRACTION PROBLEMS

P. J. CLARK, P. BETTESS, G. E. HEARN AND M. J. DOWNIE

Offshore Research Group, Department of Marine Technology, The University of Newcastle upon Tyne, Newcastle upon Tyne NE1 7RU, U.K.

SUMMARY

A new finite-element based method of calculating non-linear wave loads on offshore structures in extreme seas is presented in this paper. The diffraction wave field is modelled using Stokes wave theory developed to second order. Wave loads and free surface elevations are obtained for fixed surface-piercing structures by solving a boundary value problem for the second-order velocity potential. Special attention has been given to the radiation condition for the second-order diffraction field. Results are presented for three test examples, the vertical cylinders of Kim and Yue and of Chakrabarti, and an elliptic cylinder. These results demonstrate that early problems with the application of second-order theory arising from inadequate radiation conditions have been overcome.

KEY WORDS Stokes waves Non-linear waves Second order waves Wave diffraction Finite elements Wave loading

1. INTRODUCTION

This paper treats the prediction of non-linear water wave diffraction by fixed offshore structures using the finite element method. An offshore structure is designed to withstand the largest wave loading that it might experience during its operational life. The effect of wave diffraction on hydrodynamic loading becomes significant when a typical horizontal dimension of the structure, D say, is of comparable size to the wavelength L, i.e. $D/L > 0{\cdot}2$.

Viscous forces are small in this regime so the hydrodynamic loading is assumed to arise from the action of an ideal fluid. However, even under this hypothesis, closed-form solutions for simple configurations cannot be found because the free surface boundary condition is non-linear and the location of the free surface at any instant is unknown. These difficulties are overcome in linear water wave theory by reducing the free surface boundary condition to a Cauchy–Poisson condition on the still-water plane. Considerable success has been achieved using linear theory. Analytical solutions are available for simple configurations such as the vertical circular cylinder solution of Havelock.[1] More general structures are analysed using numerical methods, of which the boundary integral method based on Green functions[2,3] and the finite element method[4,5] have proved most popular. For reviews of this subject see References 6 and 7.

Model tests have shown that, in general, these methods predict forces well.[8,9] However, linear theory tends to underestimate the diffraction force and it has been noticed that for steep waves the error can be significant.[10] A systematic series of model tests on circular cylinders and square

0271–2091/91/040343–25$12.50

Received February 1990

caissons by Mogridge and Jamieson[11,12] showed that the discrepancy between measured and predicted forces increases steadily with wave steepness.

Stokes wave theory provides a natural framework in which to improve the modelling of wave diffraction. Here the velocity potential is decomposed into time-harmonic components and expanded in a perturbation series. By this means the influence of the non-linear free surface can be represented by a set of successive approximations. No existence or uniqueness theorems exist for a 'Stokes' diffraction theory, nor have the conditions under which converged solutions may be obtained been established. However, it is reasonable to think that if the incident wave is satisfactorily defined then so will be the diffraction wave field, and the series is expected to converge because the diffraction wave attenuates as it propagates away from the scattering body. The theory does not comfortably extend beyond second order (two terms in the Stokes expansion) because the decomposition of the velocity potential into its time harmonics is no longer 'synchronized' with its perturbation expansion. This gives rise to time-dependent secular terms in the solution,[13] causing it to become unstable. Fortunately, considerable progress can be made with second-order theory and most of the literature on non-linear wave diffraction is based on this theory.

Early attempts to solve the second-order problem failed to appreciate that the free surface boundary condition is incompatible with the boundary condition on the scattering surface.[14] As a consequence there is more than one type of wave component in the second-order diffraction field, a fact first recognized by Molin.[15] At that time determining the second-order wave force was the main objective, and an ingenious method which avoids the need to calculate the second-order velocity potential was proposed by Lighthill[16] and Molin.[15] Early difficulties in implementing this method have been largely overcome.[17,18] An alternative approach using integral transform theory was pioneered by Hunt and Baddour.[19] More recently, integral transform theory has been used to confirm that the behaviour of the second-order diffraction system in the far field has the character described by Molin's asymptotic analysis.[15,20]

Numerical methods for finding the second-order velocity potential directly were hampered by the lack of suitable radiation conditions.[21] Much effort has been devoted to this issue, and although not completely resolved, satisfactory approximations now exist. The latest methods can determine the free surface elevation, wave run-up and surface pressure distributions in addition to the peak values of wave forces.[22–24]

In this paper a direct method for calculating the second-order velocity potential based on the finite element method is presented. The first section develops the boundary value problems for the first- and second-order velocity potentials. Then follows a discussion of the radiation boundary condition for the second-order problem and how it is implemented in the numerical model. The application of the finite element method to this problem is outlined. Results from this method will be presented in another paper.[25] An expanded version of this paper is available as a report.[26]

2. BASIC THEORY

2.1. *The boundary value problem*

The co-ordinate system has its origin at the centroid of the scattering body in the plane of the undisturbed water surface. It is convenient to use both a right-handed Cartesian system (x, y, z) and a cylindrical polar system (r, θ, z) in which the z-co-ordinate is taken vertically upwards. The fluid domain V is bounded by the free surface, S_F, defined by the free surface elevation $z = \Xi(x, y, t)$ where t is the time, the seabed S_B, defined by the water depth $z = d(x, y)$, and the wetted surface of the scattering body, S_W. The domain is truncated at a 'radiation' boundary S_R,

which is an imaginary vertical cylinder, radius $r = r_\infty$, separating the inner region from the far field; see Figure 1. The still-water surface is designated by S_0. The incident wave is assumed to travel along the positive x-axis. Under the ideal fluid hypothesis, the velocity of the fluid, $\mathbf{v} = (u, v, w)$, at a point in the fluid domain, $\mathbf{r} = (x, y, z)$, is related to the velocity potential $\Phi(\mathbf{r}, t)$ by

$$\mathbf{v}(\mathbf{r}, t) = \left(\frac{\partial\Phi}{\partial x}, \frac{\partial\Phi}{\partial y}, \frac{\partial\Phi}{\partial z}\right)(\mathbf{r}, t) = \nabla\Phi(\mathbf{r}, t). \tag{1}$$

The governing equation of the fluid is Laplace's equation

$$\nabla^2\Phi = 0, \tag{2}$$

with no flow across the boundaries of the scattering body or seabed,

$$\frac{\partial\Phi}{\partial n} = 0, \tag{3}$$

where $\mathbf{n}$ is the unit normal pointing out of the fluid domain.

The dynamic and kinematic boundary conditions on the free surface can be expressed in terms of the velocity potential alone by the equation

$$\frac{\partial^2\Phi}{\partial t^2} + g\frac{\partial\Phi}{\partial z} + 2\nabla\Phi\cdot\nabla\frac{\partial\Phi}{\partial t} + \tfrac{1}{2}\nabla\Phi\cdot\nabla(\nabla\Phi\cdot\nabla\Phi) = 0. \tag{4}$$

The non-linear free surface condition on S_F is reduced to a set of boundary conditions on the still-water plane S_0 by the method of Stokes.[6,9] The velocity potential Φ is expanded in a Taylor series about $z = 0$, giving

$$\Phi(x, y, \Xi, t) = \Phi(x, y, 0, t) + \Xi\left(\frac{\partial\Phi}{\partial z}\right)_{z=0} + \frac{\Xi^2}{2}\left(\frac{\partial^2\Phi}{\partial z^2}\right)_{z=0} + \ldots. \tag{5}$$

To express this condition entirely in terms of the velocity potential, Ξ must be eliminated. The free surface elevation is found from Bernoulli's equation applied at the free surface,

$$\frac{\partial\Phi}{\partial t} + \tfrac{1}{2}(\nabla\Phi)^2 + g\Xi = 0, \tag{6}$$

where g is the gravitational constant. The equation resulting from the substitution of equations (5) and (6) into (4) is made tractable by replacing Φ with a perturbation series,

$$\Phi = \varepsilon\Phi^{(1)} + \varepsilon^2\Phi^{(2)} + O(\varepsilon^3), \tag{7}$$

where the perturbation parameter ε is the wave slope of the incident wave. In addition, the velocity potential is assumed to be made up of a set of time-harmonic components based on the angular frequency of the incident wave, ω, together with a non-periodic component. These components are related to the perturbation potentials to second order as follows:

$$\varepsilon\Phi^{(1)}(\mathbf{r}, t) = \mathrm{Re}\{\phi^{(1)}(\mathbf{r})e^{-i\omega t}\}, \tag{8a}$$

$$\varepsilon^2\Phi^{(2)}(\mathbf{r}, t) = \mathrm{Re}\{\phi^{(2)}(\mathbf{r})e^{-i2\omega t}\} - g\bar{\eta}_1^{(2)}t. \tag{8b}$$

The reduced potentials $\phi^{(1)}$ and $\phi^{(2)}$ are complex-valued functions. The second term on the right-hand side of equation (8b) eliminates the Bernoulli 'constant' from Bernoulli's equation, where $\bar{\eta}_1^{(2)}$ is the wave set-down far away from the body. If the seabed is a plane surface at $z = -d$, the

wave set-down is

$$\bar{\eta}_{\mathrm{I}}^{(2)} = \frac{-\varepsilon^2}{2k\sinh 2kd}, \qquad \varepsilon = \frac{kH}{2}, \tag{9}$$

and the velocity potentials for the incident wave are[6]

$$\phi_{\mathrm{I}}^{(1)} = -\mathrm{i}\left(\frac{H}{2}\right)\frac{g}{\omega}\frac{\cosh k(z+d)}{\cosh kd}\mathrm{e}^{\mathrm{i}kx}, \tag{10a}$$

$$\phi_{\mathrm{I}}^{(2)} = -\mathrm{i}\frac{3}{8}\left(\frac{H}{2}\right)^2\omega\frac{\cosh 2k(z+d)}{\sinh^4 kd}\mathrm{e}^{\mathrm{i}2kx}, \tag{10b}$$

where H is the height of the incident wave and k is the wave number found from the dispersion equation

$$\omega^2 = gk\tanh kd. \tag{11}$$

These potentials are subtracted from the total potential, leaving a pair of boundary value problems for the first- and second-order diffraction potentials $\phi_{\mathrm{D}}^{(1)}$, $\phi_{\mathrm{D}}^{(2)}$ respectively[17] in the form

$$\nabla^2\phi_{\mathrm{D}}^{(1)} = 0, \qquad \mathbf{r}\in V, \tag{12a}$$

$$\frac{\partial\phi_{\mathrm{D}}^{(1)}}{\partial n} = -\frac{\partial\phi_{\mathrm{I}}^{(1)}}{\partial n}, \qquad \mathbf{r}\in S_{\mathrm{W}}, \tag{12b}$$

$$\frac{\partial\phi_{\mathrm{D}}^{(1)}}{\partial z} = 0, \qquad \mathbf{r}\in S_{\mathrm{B}}, \tag{12c}$$

$$\frac{\partial\phi_{\mathrm{D}}^{(1)}}{\partial z} - \frac{\omega^2}{g}\phi_{\mathrm{D}}^{(1)} = 0, \qquad \mathbf{r}\in S_0, \tag{12d}$$

$$\lim_{r\to\infty}\frac{\partial\phi_{\mathrm{D}}^{(1)}}{\partial r} - \mathrm{i}k\phi_{\mathrm{D}}^{(1)} = o(r^{-1/2}) \tag{12e}$$

and

$$\nabla^2\phi_{\mathrm{D}}^{(2)} = 0, \qquad \mathbf{r}\in V, \tag{13a}$$

$$\frac{\partial\phi_{\mathrm{D}}^{(2)}}{\partial n} = -\frac{\partial\phi_{\mathrm{I}}^{(2)}}{\partial n}, \qquad \mathbf{r}\in S_{\mathrm{W}}, \tag{13b}$$

$$\frac{\partial\phi_{\mathrm{D}}^{(2)}}{\partial z} = 0, \qquad \mathbf{r}\in S_{\mathrm{B}}, \tag{13c}$$

$$\frac{\partial\phi_{\mathrm{D}}^{(2)}}{\partial z} - \frac{4\omega^2}{g}\phi_{\mathrm{D}}^{(2)} = \alpha_{\mathrm{D}}^{(2)}, \qquad \mathbf{r}\in S_0, \tag{13d}$$

where the free surface forcing function $\alpha_{\mathrm{D}}^{(2)}$ is given by

$$\alpha_{\mathrm{D}}^{(2)} = \alpha_{\mathrm{DI}}^{(2)} + \alpha_{\mathrm{DD}}^{(2)},$$

$$\alpha_{\mathrm{DI}}^{(2)} = -\mathrm{i}\frac{\omega}{2g}\phi_{\mathrm{D}}^{(1)}\left(\frac{\partial^2\phi_{\mathrm{I}}^{(1)}}{\partial z^2} - \nu\frac{\partial\phi_{\mathrm{I}}^{(1)}}{\partial z}\right) - \mathrm{i}\frac{\omega}{2g}\phi_{\mathrm{I}}^{(1)}\left(\frac{\partial^2\phi_{\mathrm{D}}^{(1)}}{\partial z^2} - \nu\frac{\partial\phi_{\mathrm{D}}^{(1)}}{\partial z}\right) + \mathrm{i}\frac{2\omega}{g}\nabla\phi_{\mathrm{I}}^{(1)}\cdot\nabla\phi_{\mathrm{D}}^{(1)},$$

$$\alpha_{\mathrm{DD}}^{(2)} = -\mathrm{i}\frac{\omega}{2g}\phi_{\mathrm{D}}^{(1)}\left(\frac{\partial^2\phi_{\mathrm{D}}^{(1)}}{\partial z^2} - \nu\frac{\partial\phi_{\mathrm{D}}^{(1)}}{\partial z}\right) + \mathrm{i}\frac{\omega}{g}(\nabla\phi_{\mathrm{D}}^{(1)})^2, \tag{13e}$$

with

$$\nu = \omega^2/g. \tag{14}$$

A radiation condition is required. This is discussed in Section 3.

2.2. *Hydrodynamic forces*

In this section the formulae for hydrodynamic forces are presented to second order; for details of their derivation see Reference 26. The hydrodynamic loads on a fixed body due to wave diffraction are obtained by integrating the pressure p over the wetted surface of the body, S_W. The wetted surface of a surface-piercing body is split into two parts—a mean wetted surface S_{W_0}, and a variable part ΔS_W which accounts for the changing immersion of the body through the action of the wave system:

$$S_W = S_{W_0} \cup \Delta S_W. \tag{15}$$

S_{W_0} is taken to the still-water level, $z = 0$.

$$\mathbf{f} = -\int_{S_W} p\mathbf{n}\, dS, \tag{16}$$

$$\mathbf{m} = -\int_{S_W} p(\mathbf{r} \times \mathbf{n})\, dS, \tag{17}$$

where the pressure comes from Bernoulli's equation and the unit normal $\mathbf{n}$ points into the body. The forces and moments can be expanded in a Stokes series as

$$\mathbf{f} = \varepsilon \mathbf{f}^{(1)} + \varepsilon^2 \mathbf{f}^{(2)} + O(\varepsilon^3), \tag{18a}$$

$$\varepsilon \mathbf{f}^{(1)} = \mathrm{Re}\{\mathbf{F}^{(1)} e^{-i\omega t}\}, \tag{18b}$$

$$\varepsilon^2 \mathbf{f}^{(2)} = \mathrm{Re}\{\mathbf{F}^{(2)} e^{-i2\omega t}\} + \bar{\mathbf{F}}^{(2)}, \tag{18c}$$

where the second-order force is made up of a steady drift force and an oscillatory force pulsating at the double frequency. The first-order force is given by

$$\mathbf{F}^{(1)} = i\omega\rho \int_{S_{W_0}} \phi^{(1)} \mathbf{n}\, dS. \tag{19}$$

The second-order force is made up of contributions from first- and second-order potentials:

$$\mathbf{F}^{(2)} = \mathbf{F}_1^{(2)} + \mathbf{F}_2^{(2)}, \tag{20a}$$

$$\mathbf{F}_2^{(2)} = i2\omega\rho \int_{S_{W_0}} \phi^{(2)} \mathbf{n}\, dS. \tag{20b}$$

The first-order potential is responsible for two components, one due to the dynamic pressure, the other due to the change in pressure arising from the varying immersion at the water surface:

$$\mathbf{F}_1^{(2)} = \frac{\rho}{4} \int_{S_{W_0}} (\nabla \phi^{(1)})^2 \mathbf{n}\, dS + \frac{\rho\omega^2}{4g} \oint_{C_W} (\phi^{(1)})^2 \frac{\mathbf{n}}{\sqrt{(1 - n_z^2)}}\, dC, \tag{20c}$$

where n_z is the vertical component of the unit normal at the waterline. For wall-sided bodies $n_z = 0$.

The drift forces arise from the first-order potentials only:

$$\bar{\mathbf{F}}^{(2)} = \frac{\rho}{4}\int_{S_{W_0}} (\nabla\phi^{(1)})\cdot(\nabla\phi^{(1)*})\mathbf{n}\,\mathrm{d}S - \frac{\rho\omega^2}{4g}\oint_{C_W} \phi^{(1)}\phi^{(1)*}\frac{\mathbf{n}}{\sqrt{(1-n_z^2)}}\mathrm{d}C + \mathbf{e}_z\rho g\bar{\eta}_I^{(2)}\int_{S_{W_0}} n_z\,\mathrm{d}S, \tag{21}$$

where $\mathbf{e}_z$ is the unit vector in the vertical direction. The last integral gives a vertical 'drift' force due to the Bernoulli constant. For wall-sided bodies this value is zero.

Similar expressions can be derived for the hydrodynamic moments $\mathbf{m}$ by replacing $\mathbf{n}$ in the force integrals by $\mathbf{r}\times\mathbf{n}$. The lever arm is taken about axes through the centroid of the cross-section at the base of the structure.

Expressions for the free surface elevation to second order may be found in References 6, 9 and 26.

3. RADIATION CONDITIONS FOR SECOND-ORDER DIFFRACTION

Wave problems require a suitable radiation condition to guarantee a unique solution. Since most numerical methods are truncated at an outer 'radiation' boundary, a numerical boundary condition can usually be derived from the analytical form of the radiation condition. For the first-order boundary value problem the Sommerfeld condition is the appropriate choice:

$$\lim_{r\to\infty}\frac{\partial\phi_D^{(1)}}{\partial r} - \mathrm{i}k\phi_D^{(1)} = o(r^{-1/2}). \tag{22}$$

The second-order problem requires more sophisticated treatment. Early work on the subject attempted to use a Sommerfeld condition of the form

$$\lim_{r\to\infty}\frac{\partial\phi_D^{(2)}}{\partial r} - \mathrm{i}k^{(2)}\phi_D^{(2)} = o(r^{-1/2}), \tag{23}$$

where the wave number $k^{(2)}$ was interpreted in various ways. However, this equation is not adequate, and it was not until Molin devised a physical model for the second-order wave field that a satisfactory treatment of the problem was possible.[15] In Molin's model, besides the incident wave, there are three propagating disturbances and their associated evanescent wave modes. The second-order problem is characterized by the inhomogeneous free surface condition, which contains a forcing function $\alpha^{(2)}$. The forcing function is made up of products of the first-order potentials (and their derivatives) and so can be separated into three components,

$$\alpha^{(2)} = \alpha_{II}^{(2)} + \alpha_{DD}^{(2)} + \alpha_{DI}^{(2)}, \tag{24}$$

where $\alpha_{DD}^{(2)}$ and $\alpha_{DI}^{(2)}$ are defined by equations (13e) and $\alpha_{II}^{(2)}$ is similar to $\alpha_{DD}^{(2)}$ with $\phi_I^{(1)}$ replacing $\phi_D^{(1)}$.

The term $\alpha_{II}^{(2)}$ is responsible for the second-order incident wave potential, whilst the last two terms are associated with second-order diffraction potentials, denoted by $\phi_{DD}^{(2)}$ and $\phi_{DI}^{(2)}$ respectively. The disturbances described by $\phi_{DD}^{(2)}$ and $\phi_{DI}^{(2)}$ are called locked waves by Molin and are particular solutions of Laplace's equation satisfying the inhomogeneous free surface condition and the seabed condition. The third diffraction wave in Molin's model is a linear wave (i.e. satisfying a homogeneous free surface condition) called the 'free' wave. This wave is created at the scattering surface owing to a mismatch in surface flux between the incident wave and the locked waves. It satisfies a second-order dispersion equation

$$4\omega^2 = gk_f\tanh k_f d, \tag{25}$$

where k_f is the wave number of the free wave. The incident, locked and free wave components all decay at different rates with water depth, and so evanescent wave modes are always present in the second-order problem, even when there are no evanescent wave modes in the first-order problem. These wave modes are associated with the free wave. If evanescent wave modes exist at first order they generate extra components in the forcing function $\alpha^{(2)}$, giving rise to non-linear evanescent wave modes and disturbances governed by the interaction of the evanescent and progressive wave components. The complicated wave field resulting from these interactions is best resolved by a numerical method. However, most evanescent wave modes decay rapidly away from the surface of the body and so they are not considered further.

To define a radiation condition at second order, the three components into which the diffraction potential has been decomposed are considered separately. The free wave satisfies the Sommerfeld radiation condition, equation (23), with $k^{(2)} = k_f$. However, developing radiation conditions for the locked waves is closely related to finding asymptotic approximations to the particular solutions in the far field. Indeed, such solutions are necessary if an explicit radiation condition is to be derived for the total diffraction potential, as discussed in Section 4.2.

A far-field approximation for the locked wave potentials can be developed using an asymptotic expansion in powers of $(1/kr)^{1/2}$. This has been done by Scolan.[27] The first-order diffraction potential is written as a series of Hankel functions. A standard asymptotic expansion is substituted for the Hankel functions. The free surface forcing function can then be written in terms of an asymptotic series in $(1/kr)^{1/2}$. Substituting the asymptotic expansion of the locked wave potential into Laplace's equation gives a set of differential equations in the vertical co-ordinate which are solved using the free surface and seabed boundary conditions. A similar analysis is presented in Reference 26 in which the first-order diffraction potential is retained in its original form and its radial derivative is replaced by a cylindrical damper approximation (this type of approximation is discussed in Section 4). These equations are more suitable for use with the finite element method and the first two terms are given below.

$$\left(\frac{-ig}{\omega k^2}\right)\phi_{DI}^{(2)} = \frac{A_1}{\sigma}\cosh k_{DI}(z+d)\,\phi_I^{(1)}\,\phi_D^{(1)}$$

$$+\left(\frac{1}{kr}\right)\left(\frac{A_2}{\sigma}\cosh k_{DI}(z+d)+\frac{A_4}{\sigma}k^2(z+d)^2\,S(k_{DI}(z+d))\right.$$

$$\left.+\frac{A_6}{\sigma}k^2(z+d)^2\cosh k_{DI}(z+d)\right)\phi_I^{(1)}\,\phi_D^{(1)}+\left(\frac{1}{kr}\right)\left(\frac{A_3}{\sigma}\cosh k_{DI}(z+d)\right.$$

$$\left.+\frac{A_5}{\sigma}k^2(z+d)^2\,S(k_{DI}(z+d))\right)\phi_I^{(1)}\frac{\partial\phi_D^{(1)}}{\partial\theta}, \tag{26a}$$

where

$$S(k_{DI}(z+d)) = \frac{\sinh k_{DI}(z+d)}{k_{DI}(z+d)} \tag{26b}$$

and

$$k_{DI} = k\sqrt{(2+2\cos\theta)} = 2k\cos\theta/2. \tag{26c}$$

The function S has been defined to ensure $S(0) = 1$, so avoiding unbounded coefficients near

$k_{DI} = 0$. The coefficients are defined by

$$A_1(\theta) = 3\tanh^2 kd - 1 - 2\cos\theta, \tag{26d}$$

$$A_2(\theta) = -\mathrm{i}\cos\theta - \sigma_2(\theta)A_4(\theta) - \sigma_3(\theta)A_6(\theta), \tag{26e}$$

$$A_3(\theta) = -\mathrm{i}2\sin\theta - \sigma_2(\theta)A_5(\theta), \tag{26f}$$

$$A_4(\theta) = \mathrm{i}(1+\cos\theta)\left(2(1-\cos\theta) + \frac{A_1}{4}(\theta)[1 + 4\sigma_2(\theta)(1-\cos\theta)]\right), \tag{26g}$$

$$A_5(\theta) = \mathrm{i}\sin\theta\, A_1(\theta), \tag{26h}$$

$$A_6(\theta) = -\frac{\mathrm{i}}{4}(1-\cos\theta)A_1(\theta) \tag{26i}$$

and

$$\sigma(\theta) = k_{DI}\sinh k_{DI}d - 4\nu\cosh k_{DI}d, \tag{26j}$$

$$\sigma_2(\theta) = \frac{k^2 d}{\sigma(\theta)}[(1-4\nu d)S(k_{DI}d) + \cosh k_{DI}d], \tag{26k}$$

$$\sigma_3(\theta) = (kd)^2\left(1 + 2\frac{\cosh k_{DI}d}{\sigma(\theta)d}\right). \tag{26l}$$

The other locked wave diffraction potential is given by

$$\left(\frac{-\mathrm{i}g}{\omega k^2}\right)\phi_{DD}^{(2)} = B_1\cosh 2k(z+d)\,(\phi_D^{(1)})^2 + \left(\frac{1}{kr}\right)[B_2\cosh 2k(z+d) + B_3 k(z+d)\sinh 2k(z+d)]\,(\phi_D^{(1)})^2, \tag{27a}$$

with

$$B_1 = \frac{3\nu}{8k^2\sinh^4 kd}, \tag{27b}$$

$$B_2 = \mathrm{i}\frac{1}{4\nu\sinh^2 kd} + \mathrm{i}\frac{3[(1-4\nu d)\sinh 2kd + 2kd\cosh 2kd]}{64k\sinh^6 kd}, \tag{27c}$$

$$B_3 = \mathrm{i}\frac{3\nu}{16k^2\sinh^4 kd}. \tag{27d}$$

The next section explains how the radiation condition is used to derive a numerical boundary condition for use with the finite element method.

4. CYLINDRICAL DAMPERS

4.1. High-order dampers

On the radiation boundary a boundary condition which ensures the diffraction wave has an outward flux is necessary. In the present formulation the cylindrical damper approximation of Bayliss and Turkel is used, which is explained in more detail in Reference 28.

The first-order cylindrical damper approximation to the radiation condition is

$$\frac{\partial \phi_D^{(1)}}{\partial r} \sim \left(ik - \frac{1}{2r} \right) \phi_D^{(1)}. \tag{28}$$

The second-order cylindrical damper is

$$\frac{\partial \phi_D^{(1)}}{\partial r} \sim -\beta_1^{(1)} \phi_D^{(1)} + \beta_2^{(1)} \frac{\partial^2 \phi_D^{(1)}}{\partial s^2}, \tag{29a}$$

$$\beta_1^{(1)} = \left(\frac{3}{4r^2} - i\frac{3k}{r} - 2k^2 \right) \beta_2^{(1)}, \tag{29b}$$

$$\beta_2^{(1)} = \frac{1}{2/r - 2ik}, \tag{29c}$$

where s is the tangential co-ordinate, given by $s = r\theta$, and on the radiation boundary $r = r_\infty$.

4.2. *Application of dampers to second-order diffraction*

The radiation condition for the second-order velocity potential is derived using the asymptotic far-field equations for the locked waves, equations (26) and (27). The asymptotic locked wave equations can be written as

$$\phi_{DI}^{(2)} \sim \left[a_1 + \left(\frac{1}{kr} \right) a_2 \right] \phi_I^{(1)} \phi_D^{(1)} + \left(\frac{1}{kr} \right) a_3 \phi_I^{(1)} \frac{\partial \phi_D^{(1)}}{\partial \theta}, \tag{30a}$$

$$\phi_{DD}^{(2)} \sim \left[b_1 + \left(\frac{1}{kr} \right) b_2 \right] (\phi_D^{(1)})^2, \tag{30b}$$

and their radial derivatives as

$$\frac{\partial \phi_{DI}^{(2)}}{\partial r} \sim \left[a_1 + \left(\frac{1}{kr} \right) a_2 \right] \left(\frac{\partial \phi_I^{(1)}}{\partial r} \phi_D^{(1)} + \phi_I^{(1)} \frac{\partial \phi_D^{(1)}}{\partial r} \right) + \left(\frac{1}{kr} \right) a_3 \left[\frac{\partial \phi_I^{(1)}}{\partial r} \frac{\partial \phi_D^{(1)}}{\partial \theta} + \phi_I^{(1)} \frac{\partial}{\partial \theta} \left(\frac{\partial \phi_D^{(1)}}{\partial r} \right) \right] + O(kr^{-5/2}), \tag{31a}$$

$$\frac{\partial \phi_{DD}^{(2)}}{\partial r} \sim 2 \left[b_1 + \left(\frac{1}{kr} \right) b_2 \right] \phi_D^{(1)} \frac{\partial \phi_D^{(1)}}{\partial r} + O(kr^{-3}). \tag{31b}$$

The radial derivatives of $\phi_I^{(1)}$ and $\phi_D^{(1)}$ are substituted in equation (31). The radial derivative of $\phi_D^{(1)}$ is approximated by the first-order cylindrical damper, equation (28), giving

$$\frac{\partial \phi_{DI}^{(2)}}{\partial r} \sim \left(ik(1 + \cos\theta) - \frac{1}{2r} \right) \phi_{DI}^{(2)} + O(kr^{-5/2}), \tag{32a}$$

$$\frac{\partial \phi_{DD}^{(2)}}{\partial r} \sim \left(i2k - \frac{1}{r} \right) \phi_{DD}^{(2)} + O(kr^{-3}). \tag{32b}$$

The free wave satisfies the first-order cylindrical damper

$$\frac{\partial \phi_{DF}^{(2)}}{\partial r} \sim \left(ik_f - \frac{1}{2r} \right) \phi_{DF}^{(2)}. \tag{33}$$

The normal velocity of the second-order diffraction potential on the radiation boundary is

$$\frac{\partial\phi_D^{(2)}}{\partial r} = \frac{\partial\phi_{DF}^{(2)}}{\partial r} + \frac{\partial\phi_{DI}^{(2)}}{\partial r} + \frac{\partial\phi_{DD}^{(2)}}{\partial r}$$

$$\sim \left(ik_f + \frac{1}{2r}\right)\phi_{DF}^{(2)} + \left(ik(1+\cos\theta) - \frac{1}{2r}\right)\phi_{DI}^{(2)} + \left(i2k - \frac{1}{r}\right)\phi_{DD}^{(2)}. \tag{34}$$

Writing $\phi_{DF}^{(2)}$ in equation (34) in terms of the other diffraction potentials gives

$$\frac{\partial\phi_D^{(2)}}{\partial r} \sim \left(ik_f - \frac{1}{2r}\right)\phi_D^{(2)} + [ik(1+\cos\theta) - ik_f]\,\phi_{DI}^{(2)} + \left(i2k - ik_f - \frac{1}{2r}\right)\phi_{DD}^{(2)}. \tag{35}$$

5. VARIATIONAL EQUATIONS

The variational equations for the boundary value problems, equations (12) and (13), are given in terms of the complex energy functionals $E^{(1)}(\phi_D^{(1)})$ and $E^{(2)}(\phi_D^{(2)})$:[29]

$$2E^{(1)}(\phi_D^{(1)}) = \tfrac{1}{2}\int_V (\nabla\phi_D^{(1)})^2\,dV + \int_{S_W} \phi_D^{(1)}\frac{\partial\phi_I^{(1)}}{\partial n}\,dS - \frac{\nu}{2}\int_{S_0} (\phi_D^{(1)})^2\,dS$$

$$+ \tfrac{1}{2}\int_{S_R}\left[\beta_1^{(1)}(\phi_D^{(1)})^2 + \beta_2^{(1)}\left(\frac{\partial\phi_D^{(1)}}{\partial s}\right)^2\right]dS, \tag{36a}$$

$$2E^{(2)}(\phi_D^{(2)}) = \tfrac{1}{2}\int_V (\nabla\phi_D^{(2)})^2\,dV + \int_{S_W} \phi_D^{(2)}\frac{\partial\phi_I^{(2)}}{\partial n}\,dS - 2\nu\int_{S_0} (\phi_D^{(2)})^2\,dS$$

$$+ \tfrac{1}{2}\int_{S_R} \beta_1^{(2)}(\phi_D^{(2)})^2 - \int_{S_R} \phi_D^{(2)}(\beta_{DI}^{(2)}\phi_{DI}^{(2)} + \beta_{DD}^{(2)}\phi_{DD}^{(2)})\,dS, \tag{36b}$$

where $\beta_{1,2}^{(1)}$ are the transmission coefficients given by equations (29) and the second-order transmission coefficients are given by

$$\beta_1^{(2)} = -ik_f + 1/2r,$$

$$\beta_{DI}^{(2)} = -ik_f + ik(1+\cos\theta),$$

$$\beta_{DD}^{(2)} = -ik_f + i2k - 1/2r.$$

These equations are solved by minimizing the functionals with respect to their velocity potentials.

6. FINITE ELEMENT EQUATIONS

An isoparametric finite element formulation is used to solve the variational equations (see e.g. Reference 29). In this formulation an element in a 'local' co-ordinate system, $\rho = (\xi, \eta, \zeta)$, is mapped to the curvilinear element in the global co-ordinate system, $\mathbf{r} = (x, y, z)$, by means of a set of 'shape' functions, $N_j^{(e)}(\rho)$, which have as their coefficients the global co-ordinates of the element nodes $\mathbf{r}_j^{(e)}$. For an element with n nodes,

$$\mathbf{r} = \sum_{j=1}^{n} N_j^{(e)}(\rho)\mathbf{r}_j^{(e)} = \{N^{(e)}\}^T\{\mathbf{r}^{(e)}\}. \tag{37}$$

The velocity potential $\phi(\mathbf{r})$ is distributed over the element in the same way:

$$\phi(\mathbf{r}) = \{N^{(e)}\}^T\{\phi^{(e)}\}. \tag{38}$$

The nodal values of the velocity potential, $\phi_j^{(e)}$, are the unknown coefficients in the final matrix equation.

The fluid velocities are found by taking the grad of the velocity potential. The Jacobian matrix $[J]$ relates grad in local co-ordinates, $\nabla_\rho = (\partial/\partial\xi, \partial/\partial\eta, \partial/\partial\zeta)$, to grad in global co-ordinates, $\nabla = (\partial/\partial x, \partial/\partial y, \partial/\partial z)$:

$$\begin{aligned}\nabla\phi(\mathbf{r}) &= [J]^{-1}[\nabla_\rho N^{(e)}]\{\phi^{(e)}\}. \\ &= [B^{(e)}]\{\phi^{(e)}\},\end{aligned} \tag{39}$$

where the Jacobian matrix is

$$[J] = [\nabla_\rho N^{(e)}]\{\mathbf{r}^{(e)}\}. \tag{40}$$

Evaluating forces on the wetted surface gives rise to integrals involving a Jacobian matrix that is not square. The treatment of this case is discussed in Reference 26.

The usual C^0 shape functions are used in the present work; these can be found in many textbooks.[29] The nodal values of the velocity potentials, $\{\phi_D^{(1)}\}$ and $\{\phi_D^{(2)}\}$, are found from the complex energy equations (36). Each integral in these equations is the sum of the corresponding element equations. For example, if there are N elements making up the fluid domain, then the total complex kinetic energy is

$$\begin{aligned}\tfrac{1}{2}\int_V (\nabla\phi_D^{(n)})^2 \, dV &= \tfrac{1}{2}\sum_{j=1}^{N} \{\phi_D^{(e)}\}_j^T [K_1^{(e)}]_j \{\phi_D^{(e)}\}_j \\ &= \tfrac{1}{2}\{\phi_D^n\}^T [K_1^{(n)}]\{\phi_D^{(n)}\}, \quad n = 1 \text{ and } 2,\end{aligned} \tag{41}$$

where the element matrix is

$$[K_1^{(e)}] = \int_{-1}^{1}\int_{-1}^{1}\int_{-1}^{1} [B^{(e)}]^T [B^{(e)}] \, |J| \, d\xi \, d\eta \, d\zeta. \tag{42}$$

The remaining integrals in equations (36) are transformed in a similar way and combined together to give the 'system' equation for the complex energy. Minimizing the complex energy gives a pair of matrix equations for the first- and second-order diffraction potentials,

$$[K^{(n)}]\{\phi_D^{(n)}\} = \{b^{(n)}\}, \quad n = 1 \text{ and } 2, \tag{43}$$

which is solved using Gaussian elimination.

Numerical approximations to the force integrals are derived using equations (38)–(40), and these can be evaluated once the velocity potentials have been found.

7. RESULTS

In this section the hydrodynamic forces on and free surface elevation around three configurations are presented. Until recently, the only results given in many papers were the hydrodynamic forces on the body. The majority of model test data give the total force, usually the absolute or average peak forces. There have been some attempts to measure the second-order force directly, which has the advantage that it removes most other non-linear effects from consideration. This will make the checking of second-order codes currently available or under development much easier. Nevertheless, the main test for the usefulness of the code is its ability to predict peak forces accurately. In the presentation of results the forces, elevations and pressures are converted to

coefficient form. Forces and moments are normalized according to

$$\mathbf{F}^{(1)} \leftarrow \frac{\mathbf{F}^{(1)}}{\frac{1}{2}\rho g a^2 H}, \qquad \mathbf{F}^{(2)} \leftarrow \frac{\mathbf{F}^{(2)}}{\frac{1}{4}\rho g a H^2},$$

$$\mathbf{M}^{(1)} \leftarrow \frac{\mathbf{M}^{(1)}}{\frac{1}{2}\rho g a^3 H}, \qquad \mathbf{M}^{(2)} \leftarrow \frac{\mathbf{M}^{(2)}}{\frac{1}{4}\rho g a^2 H^2}.$$

The surface elevation is normalized according to

$$\eta^{(1)} \leftarrow \frac{\eta^{(1)}}{H/2}, \qquad \eta^{(2)} \leftarrow \frac{\eta^{(2)}}{H^2/4a},$$

and the pressure as

$$|p^{(1)}| \leftarrow \frac{|p^{(1)}|}{\frac{1}{2}\rho g H}, \qquad |p^{(2)}| \leftarrow \frac{|p^{(2)}|}{\frac{1}{4}\rho g H^2/a},$$

where ρ is the water density and a is a characteristic horizontal dimension of the structure. For the circular cylinder a is the radius; for more general surface-piercing structures it is given by the square root of the waterplane area of the body divided by π.

In this paper three examples are treated. The first is the circular cylinder in shallow water investigated by Kim and Yue[22] and further studied by Boudet and Scolan,[30] Scolan and Molin[23] and Chau.[24] There are no model test results for this particular cylinder, but a very similar cylinder was tested by Chakrabarti[9], for which the peak forces have been presented over a range of wave frequencies. This is the second example. The last example is an elliptic cylinder, for which linear diffraction results have been obtained from a boundary integral code at Newcastle. Further results will be presented in a future paper.[25]

7.1. Preliminary checks

Before testing the code on the second-order diffraction problem, a model for a second-order propagating Stokes wave on a two-dimensional vertical sliee was studied. Apart from testing the integrity of the code, this model allowed different mesh gradings to be tried. In this model the flux was prescribed at the entrance boundary and a plane damper used to transmit the wave at the exit boundary. Formulated in this way, the wave propagation model is analagous to the diffraction problem. The position of the exit boundary was varied and it was found that the second-order solution tended to diverge along the path of propagation if fewer than 10 quadratic elements per wavelength were used to model the wave. Best results were obtained if the mesh spacing in the vertical direction was similar to the horizontal spacing. These guidelines were adopted in the diffraction work. In view of the tendency of the second-order potential to decay slowly with depth, it was decided to give the mesh equal spacing in the depth.

The diffraction problem was modelled in the following way. The first- and second-order boundary value problems are solved on the same mesh, which takes advantage of the symmetry about the centre-plane (since all the test examples are symmetrical). The meshes are based on a polar co-ordinate system with a circular outer boundary; the outer boundary is placed between one and two wavelengths from the surface of the body. A typical mesh has 10 elements per wavelength in the radial direction, and 9 elements in the circumferential direction. The number of elements in the vertical direction is chosen to give a similar spacing to the radial mesh. The spacing of nodes is usually constant in each co-ordinate direction.

The FORTRAN 77 code was developed on a SUN 3/50 workstation. A more powerful computer, a GOULD NP1, was used to study the convergence of the method, and all results in

this paper have been obtained using this machine. However, the reference test example, based on a mesh containing $10 \times 9 \times 4$ quadratic serendipity elements, could be run on a SUN (or similar) workstation.

7.2. *Kim and Yue's cylinder*

The general particulars for this cylinder are:

cylinder radius $a = 10$ m

wave depth $d = 10$ m

wave height $H = 2$ m

wave periods $T = 5{\cdot}794$, $4{\cdot}4864$ and $3{\cdot}7917$ s.

The acceleration constant is $g = 9{\cdot}807\ \mathrm{m\,s^{-2}}$ and the water density is $\rho = 1025\ \mathrm{kg\,m^{-3}}$. The choice of wave periods gives diffraction parameters $va = 1{\cdot}2$, $2{\cdot}0$ and $2{\cdot}8$.

The simplest way to assess convergence of the results is to investigate the values of the second-order forces for a variety of mesh configurations. The reference mesh is a half-annulus with $10 \times 9 \times 4$ quadratic serendipity elements in the (r, θ, z)-directions respectively (Figure 1), where the radiation boundary is located at $r = 56{\cdot}0$, $35{\cdot}0$ and $32{\cdot}3$ m, corresponding to $va = 1{\cdot}2$, $2{\cdot}0$ and $2{\cdot}8$ respectively. The radiation boundary for $va = 2$ is consistent with Scolan and Molin's choice[23] since the wavelength is $30{\cdot}4$ m. The forces and moments from the reference mesh are compared with the numerical values calculated by Kim and Yue in Table I. For each value of the force and moment the first line gives Kim and Yue's value and the second the finite element force prediction. The final line is the value of the total second-order force obtained by Kim and Yue using a semi-analytical 'indirect' method for calculating forces. This value is probably more accurate than the numerical value.

The convergence of the finite element computations is investigated by focusing on the case $va = 2$. Four issues have been considered: the fineness of the mesh, the proximity of the radiation boundary to the body, the use of simpler approximations to the radiation boundary condition, and the use of other element types. The influence of the mesh discretization was assessed by fixing

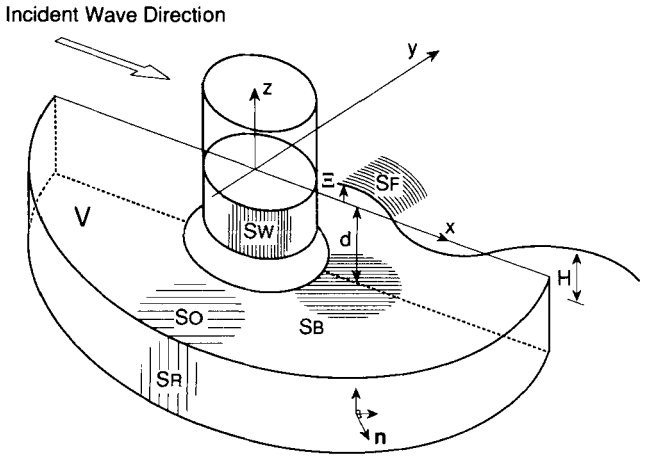

Figure 1. Co-ordinate system and labelling convention

Table I. Complex force and moment coefficients: FE versus Kim and Yue.[22] For each force the first line is Kim and Yue's numerical result and the second line the finite element result using a 10 × 9 × 4 quadratic serendipity mesh with the radiation boundaries at 56·0, 35·0 and 32·3 m respectively

		Diffraction parameter *va*		
		1·2	2·0	2·8
$F_x^{(1)}$	K&Y	0·708 −2·531	−0·264 −1·606	−0·745 −0·742
	FE	0·710 −2·532	−0·264 −1·607	−0·746 −0·743
$\bar{F}_x^{(2)}$	K&Y	0·826	0·711	0·655
	FE	0·827	0·711	0·656
$F_{x1}^{(2)}$	K&Y	−1·648 −0·305	−1·076 0·846	0·887 1·345
	FE	−1·648 −0·309	−1·096 0·850	0·893 1·342
$F_{x2}^{(2)}$	K&Y	2·258 −0·135	1·973 −1·830	−2·208 −3·604
	FE	2·249 −0·125	1·977 −1·831	−2·220 −3·601
$F_x^{(2)}$	K&Y	0·610 −0·440	0·897 −0·984	−1·321 −2·259
	FE	0·601 −0·434	0·882 −0·982	−1·327 −2·259
$F_{xIM}^{(2)}$	K&Y	0·611 −0·444	0·878 −0·986	−1·317 −2·265
$M_y^{(1)}$	K&Y	0·401 −1·431	−0·165 −1·003	−0·510 −0·509
	FE	0·401 −1·432	−0·165 −1·004	−0·511 −0·510
$\bar{M}_y^{(2)}$	K&Y	0·870	0·823	0·778
	FE	0·871	0·823	0·778
$M_{y1}^{(2)}$	K&Y	−1·485 −0·382	−1·044 0·797	0·829 1·272
	FE	−1·484 −0·386	−1·064 0·801	0·836 1·269
$M_{y2}^{(2)}$	K&Y	1·200 −0·302	1·042 −0·990	−1·360 −2·013
	FE	1·193 −0·294	1·045 −0·989	−1·367 −2·010
$M_y^{(2)}$	K&Y	−0·285 −0·684	−0·002 −0·193	−0·531 −0·741
	FE	−0·291 −0·680	−0·019 −0·188	−0·531 −0·741
$M_{yIM}^{(2)}$	K&Y	−0·284 −0·688	−0·022 −0·192	−0·525 −0·744

Table II. The effect of the number of elements in the radial direction; $va = 2$, $r_\infty = 35$ m, $N \times 9 \times 4$ quadratic serendipity mesh

	K&Y	$N = 10$	15	20
$F_{x2}^{(2)}$	1·972 −1·835	1·97733 −1·83122	1·97578 −1·83148	1·97553 −1·83132
$M_{y2}^{(2)}$	1·041 −0·993	1·04518 −0·98870	1·04369 −0·98882	1·04345 −0·98866

the overall dimensions of the mesh and systematically increasing the number of elements in each co-ordinate direction in turn, keeping the number of elements in the remaining co-ordinate directions constant. The values of the second-order force components due to the second-order velocity potential are used as the basis of comparison. The results of this study are contained in Tables II–IV. In all three tables the first column is the semi-analytical result obtained from Kim and Yue. The effect of increasing the number of elements in the radial direction is slight (Table II). Similarly, the force is little affected by changing the circumferential distribution of elements

Table III. The effect of the number of elements in the circumferential direction; $va = 2$, $r_\infty = 35$ m, $10 \times N \times 4$ quadratic serendipity mesh

	K&Y	$N=9$	12	15
$F_{x2}^{(2)}$	1·972 −1·835	1·97733 −1·83122	1·97600 −1·83210	1·97628 −1·83191
$M_{y2}^{(2)}$	1·041 −0·993	1·04518 −0·98870	1·04429 −0·98920	1·04448 −0·98909

Table IV. The effect of the number of elements in the vertical direction; $va = 2$, $r_\infty = 35$ m, $10 \times 9 \times N$ quadratic serendipity mesh

	K&Y	$N=4$	5	6	7
$F_{x2}^{(2)}$	1·972 −1·835	1·97733 −1·83122	1·97562 −1·83138	1·97532 −1·83150	1·97525 −1·83156
$M_{y2}^{(2)}$	1·041 −0·993	1·04518 −0·98870	1·04367 −0·98875	1·04341 −0·98884	1·04335 −0·98889

Table V. Comparison of reference finite element results against results using finer meshes, other element types and simpler radiation conditions; $va = 2$, $r_\infty = 35$ m except for the $15 \times 12 \times 6$ quadratic serendipity mesh where $r_\infty = 47{\cdot}5$ m

	Complex force coefficients					
	$F_x^{(1)}$	$\bar{F}_x^{(2)}$	$F_{x1}^{(2)}$	$F_{x2}^{(2)}$	$F_x^{(2)}$	$\Delta_x^{(2)}$
Quad. ser.	−0·264	0·711	−1·096	1·977	0·882	0·43
$10 \times 9 \times 4$	−1·607		0·850	−1·831	−0·982	
Quad. ser.	−0·264	0·711	−1·094	1·970	0·876	0·27
$15 \times 12 \times 6$	−1·607		0·849	−1·838	−0·989	
Pl. damp.	−0·268	0·714	−1·083	1·943	0·860	2·39
$10 \times 9 \times 4$	−1·589		0·940	−1·952	−1·012	
1st rad.	−0·266	0·709	−1·094	1·988	0·894	2·71
$10 \times 9 \times 4$	−1·607		0·870	−1·887	−1·018	
Quad. Lag.	−0·264	0·711	−1·095	1·977	0·882	0·43
$10 \times 9 \times 4$	−1·607		0·850	−1·831	−0·982	
Cub. ser.	−0·264	0·712	−1·097	1·983	0·886	1·29
$7 \times 6 \times 3$	−1·608		0·849	−1·820	−0·971	
Cub. ser.	−0·264	0·711	−1·094	1·973	0·878	0·23
$10 \times 9 \times 4$	−1·607		0·850	−1·832	−0·983	

(Table III) or the vertical distribution (Table IV). This shows that the sensitivity of the results to increasing mesh refinement is smaller than the discrepancy between different numerical solutions of the same boundary value problem. The effect of an overall finer mesh with radiation boundary taken further out is shown by the second entry to Table V, where a $15 \times 12 \times 6$ mesh is used with $r_\infty = 47{\cdot}5$ m. The percentage error in the second-order force, $\Delta_x^{(2)}$, in the final column of Table V is calculated from Kim and Yue's semi-analytical value:

$$\Delta_x^{(2)} = \left| \frac{F_x^{(2)}}{F_{x,\mathrm{IM}}^{(2)}} - 1 \right| \times 100.$$

The effect of moving the radiation boundary on the values of the second-order force is illustrated in Figure 2. The percentage error in forces and moments arising from the second-order potential alone are calculated from Kim and Yue's values in the same way as $\Delta_x^{(2)}$ defined above (replacing $F_x^{(2)}$ by $F_{x2}^{(2)}$ and $M_{y2}^{(2)}$ respectively). The radiation boundary is moved from $r/a = 1{\cdot}5$ to $r/a = 4{\cdot}0$ in 0·5 steps. The number of elements per wavelength remains constant, so the radiation boundary is moved outwards by adding new layers of elements. Convergence of the absolute value of the force to a level of accuracy suitable for engineering calculations (error less than 1%) is achieved within half a wavelength ($r/a = 2{\cdot}0$); the phase converges more slowly. However, the circular cylinder is unlikely to provide the most demanding test of the radiation condition, and setting the radiation condition at one wavelength from the surface of the body has been adopted as a useful rule of thumb provided the water depth is not great. In this work the practical limit on the size of problem is the number of finite elements in the mesh, which restricts us to depth ratios up to $d/a = 3$.

Two other checks were made on the radiation condition based on the standard mesh. In the first the quality of the cylindrical damper was assessed by replacing the cylindrical dampers in the first- and second-order diffraction problems with plane dampers. The plane damper is derived from the equation

$$\partial\phi_D/\partial n = ik\phi_D \quad \text{on } S_R,$$

where k is the appropriate wave number. In the second the asymptotic equations for the locked

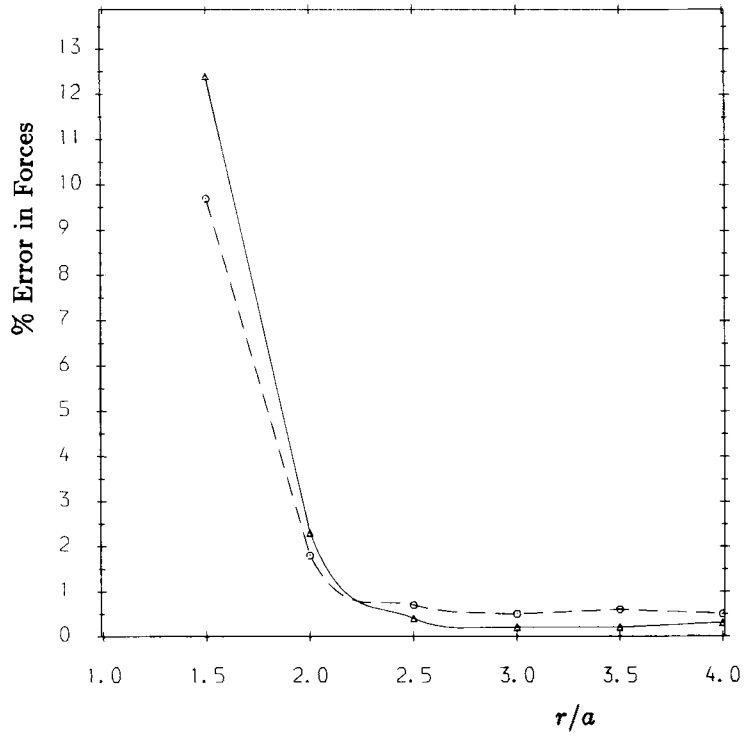

Figure 2. Rate of convergence of forces with proximity of the radiation boundary for circular cylinder $d/a = 1{\cdot}0$, $va = 2{\cdot}0$. Error in the second order horizontal force, $|F_{x2}^{(2)}/F_{x2,IM}^{(2)} - 1| \times 100\%$ (——). Error in the second order overturning moment, $|M_{y2}^{(2)}/M_{y2,IM}^{(2)} - 1| \times 100\%$ (– – –)

waves, in which the terms $o(1/kr)$ were dropped, were applied and the first-order calculation used the simple cylindrical damper, equation (28). These results appear in the third and fourth lines of Table V.

Table V also contains comparisons with two different element types. These are the quadratic Lagrange element and the cubic serendipity element. The meshes have the same element discretization as the reference mesh. Although there is no difference in the results for the quadratic Lagrange compared to the quadratic serendipity, they have been found to converge more quickly. Nevertheless, fewer degrees of freedom are required for the serendipity elements, which makes their use more cost effective. The results from the cubic elements show that for the same number of elements as used in the quadratic mesh the results are very good, but for about the same number of degrees of freedom the results are less good. This may be surprising in view of the superior interpolating qualities of the cubic, but may be related to lack of mid-face nodes in serendipity elements which compromises their ability to interpolate oscillatory functions.

The properties of the diffraction field that depend on the second-order potential include the free surface elevation and pressure distribution. The free surface elevation at the waterline of the cylinder is shown in Figure 3, where the curves come from a $10 \times 16 \times 4$ quadratic serendipity mesh and the symbols are Kim and Yue's values extracted from Figure 7 of Reference 22. Notice that the wave set-down $\bar{\eta}^{(2)}$ varies around the cylinder.

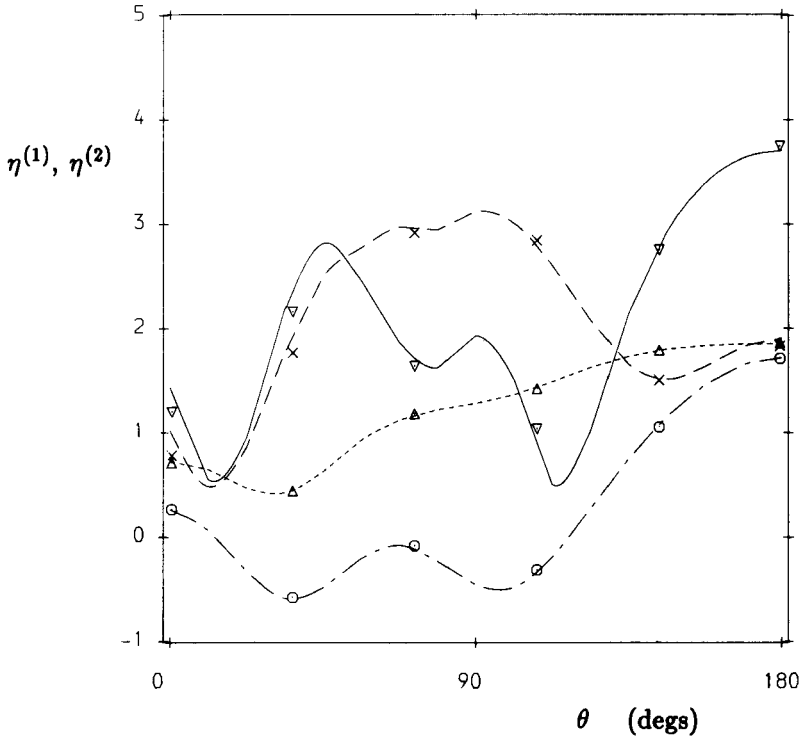

Figure 3. Modulus of the free surface elevation for circular cylinder, $d/a = 1{\cdot}0$, $va = 2{\cdot}0$. Comparison of finite element (FE) results with those of Kim and Yue[22] (K&Y). FE mesh $10 \times 16 \times 4$ quadratic serendipity elements, $r_\infty/a = 3{\cdot}5$. First order elevation, $|\eta^{(1)}|$: FE. (- - - - -), K&Y ($\triangle$). Second order elevation, $|\eta^{(2)}|$: FE. (— — —), K&Y ($\times$). Second order elevation based on $\phi^{(2)}$, $|\eta_2^{(2)}|$: FE. (——), K&Y (∇). Wave set-down, $\bar{\eta}^{(2)}$: FE. (— — —), K&Y ($\odot$)

An insight into the behaviour of the second-order diffraction potential can be gained by decomposing it into the components $\phi_{DF}^{(2)}$, $\phi_{DI}^{(2)}$ and $\phi_{DD}^{(2)}$ on the radiation boundary using the asymptotic equations for the locked waves. The imaginary parts of the component diffraction potentials on a circular contour $r = 35$ m, lying in the $z = 0$ plane, are plotted in Figure 4, which is calculated using the reference mesh. These results compare well with Figure 3 of Reference 23. The plot shows that the second-order diffraction potential is dominated by the locked wave on the weather (up-wave) side of the cylinder and by the free wave on the lee (down-wave) side.

The manner in which the dominant locked wave potential on the weather side gradually yields to the free wave on the lee side can also be seen from the free surface elevation around the cylinder due to $\phi_D^{(2)}$ alone, denoted $\eta_{D2}^{(2)}$. A contour plot of $\eta_{D2}^{(2)}$ is given in Figure 5, in which the upper half is the real part while the lower half is the imaginary part; the outer boundary is located at $r = 35$ m. The plot shows the characteristic U-shaped diffraction pattern girding the cylinder found in Figure 4 of Reference 23 (the outer boundary is $r = 70$ m in this figure). The weather side is comparatively wave-free and in this region the asymptotic equations indicate that the locked wave decays slowly with depth and does not behave much like a propagating wave. The region $150° > \theta > 80°$ exhibits strong locked wave influence, with the crests fragmented into a regular pattern of island structures, indicating interference between the locked and free wave components. Continuing around the cylinder, the diffraction pattern undergoes a change in which the locked wave field gives way to a region dominated by the free wave on the lee side of the cylinder. This is indicated by the shorter wavelength of the free wave.

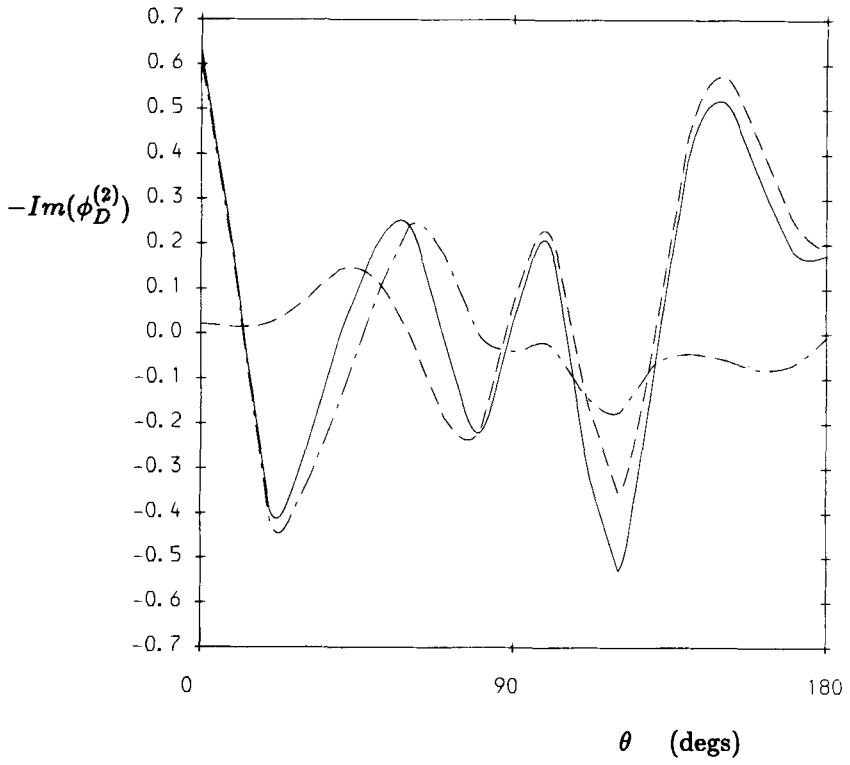

Figure 4. Imaginary parts of the second order diffraction potential on the radiation boundary $r_\infty/a = 3{\cdot}5$, $z = 0{\cdot}0$ for the circular cylinder $d/a = 1{\cdot}0$, $va = 2{\cdot}0$. FE mesh $10 \times 9 \times 4$ quadratic serendipity elements. The potentials have been multiplied by -1 to allow comparison with Figure 4 of Reference 23. $-\mathrm{Im}\{\phi_D^{(2)}\}$ (——), $-\mathrm{Im}\{\phi_{DI}^2 + \phi_{DD}^{(2)}\}$ (– – –), $-\mathrm{Im}\{\phi_{DF}^{(2)}\}$ (— — —)

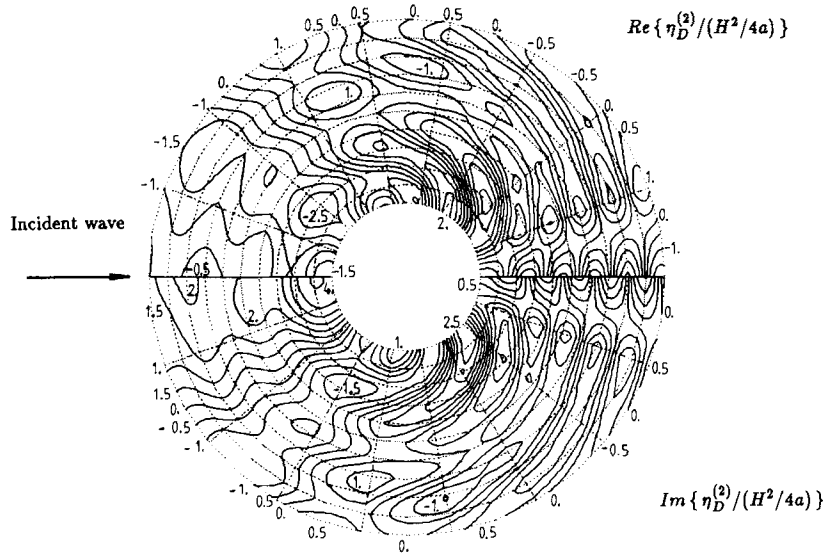

Figure 5. Contour plot of the free surface elevation due to $\phi_D^{(2)}$ around circular cylinder $d/a = 1{\cdot}0$, $va = 2{\cdot}0$. FE mesh $10 \times 9 \times 4$ quadratic serendipity elements, $r_\infty/a = 3{\cdot}5$. Each box is a finite element. The upper half is the real part of the surface elevation and the lower half the imaginary part. The contours are drawn at intervals of 0·5

Another perspective on the behaviour of the second-order velocity potential is gained by looking at the corresponding distribution of pressure on the surface of the body. The slow decay of the second-order pressure has been found in model tests by Hogben *et al.*[31] in which pressure pulses at the second harmonic were detected at the foot of a cylinder undergoing wave tests. Consequently, second-order forces reach much deeper than the first-order ones. It has been suggested that the second-order pressure acting on the underside of the buoyancy chambers of a tension leg platform, at a frequency close to one of the platform's resonant frequencies, is responsible for the phenomenon of 'springing'. The unusual behaviour of the second-order pressure is illustrated in Figures 6 and 7, which apply to the diffraction parameter $va = 1{\cdot}2$. Figure 6 shows the decay with depth of the modulus of the second-order pressure owing to the total second-order potential. The curves are the finite element results obtained from a $10 \times 16 \times 4$ quadratic serendipity mesh, $r_\infty = 56$ m, and the symbols are the values taken from Figure 4 of Reference 22. Figure 7 shows the corresponding contour plot of the second-order pressure over the surface of the cylinder. The horizontal axis is located at the base of the cylinder and the abscissa is the circumferential co-ordinate. The left-hand edge is the lee side of the cylinder and the right-hand edge the weather side. As can be seen, there is a pressure peak near the midpoint of the cylinder. This indicates that the second-order velocity potential does not decay monotonically with depth.

7.3. Chakrabarti's cylinder

The particulars of this cylinder are:

$a = 1{\cdot}0287$ m

$d/a = 1{\cdot}16$

$H/d = 0{\cdot}225$

$ka = 0{\cdot}8565$, $1{\cdot}1739$, $1{\cdot}311$, $1{\cdot}4509$ and $1{\cdot}6905$

where ka is the diffraction parameter based on wave number.

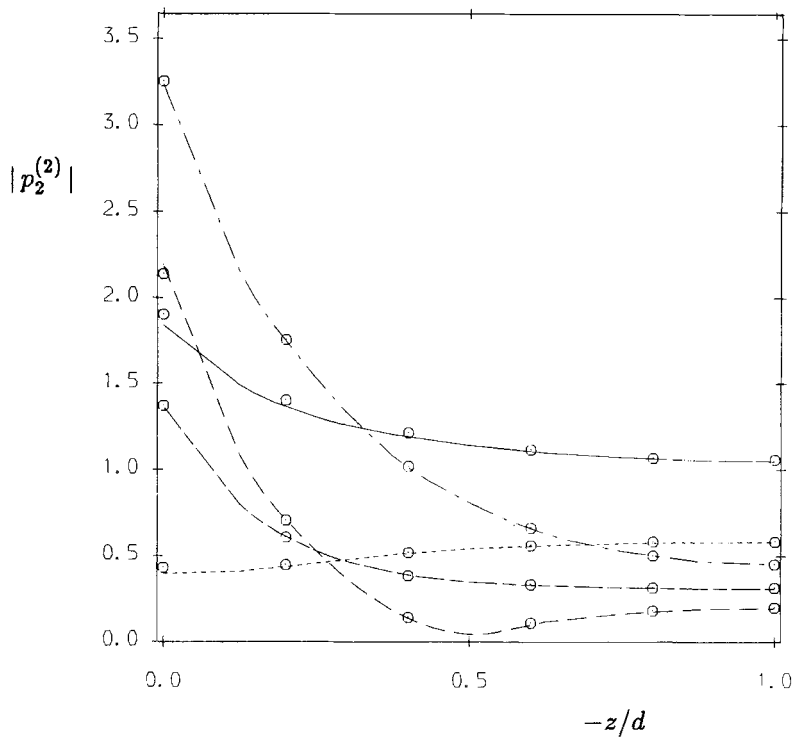

Figure 6. Modulus of the second order pressure due to $\phi^{(2)}$ on the surface of circular cylinder $d/a = 1{\cdot}0$, $va = 1{\cdot}2$. FE mesh $10 \times 16 \times 4$ quadratic serendipity elements, $r_\infty/a = 5{\cdot}6$. FE results are shown for $\theta = 0°$ (– – –), $\theta = 45°$ (———), $\theta = 90°$ (— — —), $\theta = 135°$ (-----), $\theta = 180°$ (———), the symbols (⊙) are taken from Reference 22

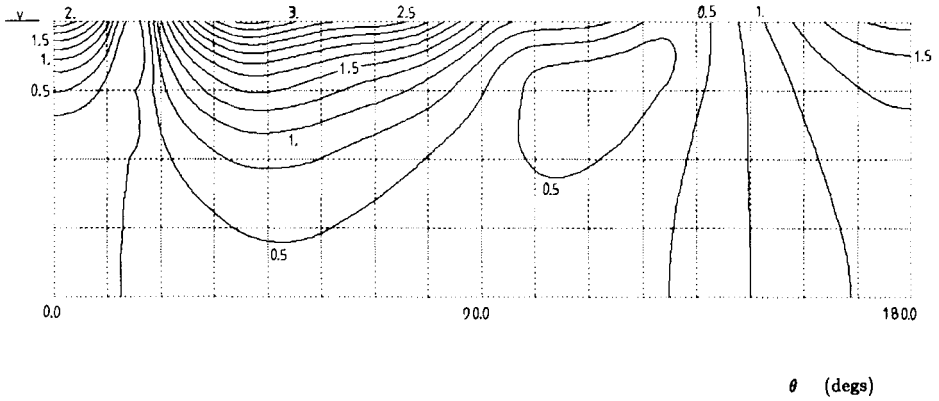

Figure 7. Contour plot of the modulus of the second order pressure due to $\phi^{(2)}$ on the same cylinder as shown in Figure 6. The free surface is at the top. The incident wave travels from right to left. Each box corresponds to a finite element. The contours are drawn at intervals of 0·25

The first- and second-order forces and the peak forces are presented in Table VI. The final column contains Chakrabarti's measured values.[10] Figure 8 shows a plot of the peak forces, comparing the calculated and measured values superimposed on the linear force curve.

The meshes used for the calculations consisted of $20 \times 9 \times 5$ quadratic serendipity elements, with the radiation boundary taken two wavelengths from the surface of the body. There are

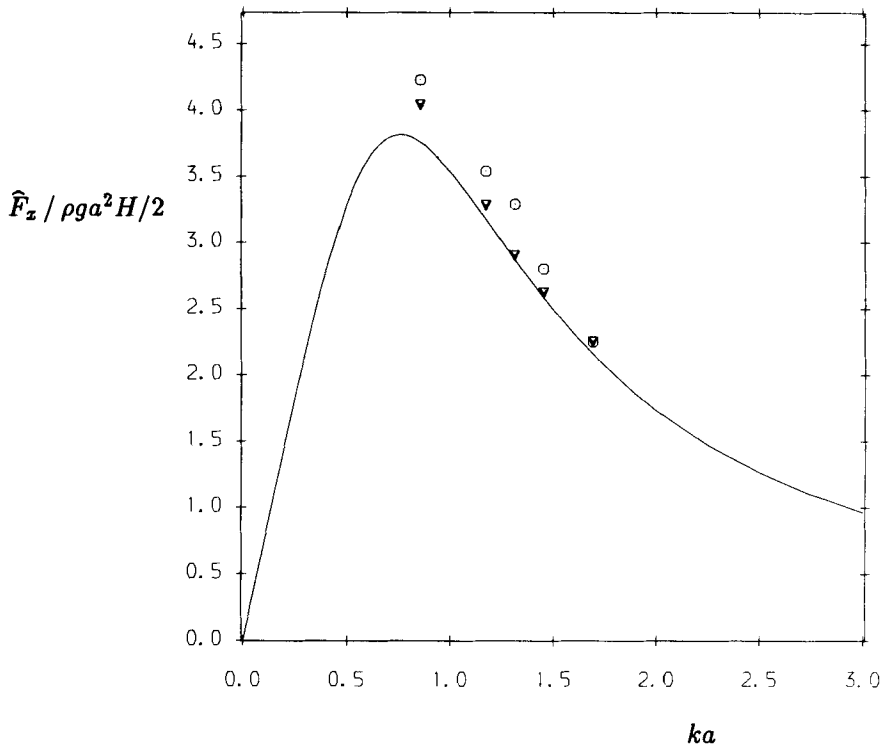

Figure 8. Diffraction force on Chakrabarti and Tam's cylinder[9], $d/a = 1{\cdot}16$, $H/d = 0{\cdot}225$. FE mesh $20 \times 9 \times 5$ quadratic serendipity elements, $r_\infty/a = 1 + 4\pi/ka$. The figure shows the linear force prediction (——), compared with the FE peak force prediction (∇) and the measured peak forces ($\odot$)

Table VI. Results for Chakrabarti's cylinder

	Complex force coefficients				
ka	$F_x^{(1)}$	$\bar{F}_x^{(2)}$	$F_x^{(2)}$	$\hat{F}_{calc}$	$\hat{F}_{meas}$
0·857	1·260 −3·540	0·990	0·218 −1·906	4·04	4·23
1·174	1·049 −2·993	0·874	0·527 −0·522	3·28	3·54
1·311	0·835 −2·746	0·797	0·868 −0·246	2·90	3·29
1·451	0·600 −2·512	0·742	1·185 −0·075	2·62	2·80
1·690	0·214 −2·144	0·704	1·474 −0·188	2·25	2·25

noticeable discrepancies between the measured and calculated forces, particularly in the middle range of wave numbers. In this middle range two effects combine to cause a small contribution from the second-order force. First, the magnitude of the second-order force falls. This is because the contribution from the first-order potentials opposes the contribution from the second-order potential, leading to substantial cancelling. Secondly, the first- and second-order forces become anti-phased so that there is little reinforcement of the peak force from the second-order part. Perhaps the higher-order wave forces make a more significant contribution. Another possibility is

the effect of tank blockage in wave diffraction model tests. Hung has shown that these can cause large discrepancies in force values at particular frequencies.[32] However, at this stage all we can say is that the non-linearities measured by Chakrabarti cannot be fully explained by second-order diffraction theory.

7.4. Elliptic cylinder

There are no numerical or experimental results for this example; it is included to give a new set of results. The choice of particulars of the cylinder, presented below, is influenced by the elliptic island of Yue *et al.*:[5]

semi-major axis $a = 2{\cdot}0$ m

semi-minor axis $b = 1{\cdot}0$ m

water depth $d = 2{\cdot}0$ m

wave height $H = 2{\cdot}0$ m

diffraction parameters $ka = 1{\cdot}0$, $2{\cdot}0$ and $3{\cdot}0$.†

The mesh is made up of $10 \times 9 \times 8$ quadratic serendipity elements and the radiation boundary is located at one wavelength from the surface of the longer axis. The incident wave travels along the same axis. The first- and second-order forces and peak forces are given in Table VII. The first-order force calculated by the boundary integral code MATTHEW, developed by Hearn at Newcastle University, is shown for comparison in the first line of this table. The free surface elevation around the waterline of the cylinder is plotted in Figure 9 and a contour plot of the surrounding free surface elevation due to the second-order potential alone, $\eta_{D2}^{(2)}$, is given in Figure 10.

Table VII. Complex force and moment coefficients for elliptic cylinder

	Diffraction parameter ka		
	1·0	2·0	3·0
$F_x^{(1)}$	0·234 −1·415 0·231 −1·414	−0·046 −0·836 −0·046 −0·837	−0·251 −0·230 −0·250 −0·231
$\bar{F}_x^{(2)}$	0·274	0·180	0·177
$F_{x1}^{(2)}$	−0·184 −0·243	−0·381 0·334	0·453 0·107
$F_{x2}^{(2)}$	0·141 −0·845	0·535 −0·472	−0·997 −0·303
$F_x^{(2)}$	−0·043 −1·088	0·154 −0·139	−0·544 −0·195
$M_y^{(1)}$	0·126 −0·761 0·124 −0·760	−0·029 −0·518 −0·029 −0·518	−0·175 −0·161 −0·174 −0·161
$\bar{M}_y^{(2)}$	0·255	0·210	0·213
$M_{y1}^{(2)}$	−0·156 −0·367	−0·363 0·322	0·425 0·111
$M_{y2}^{(2)}$	0·060 −0·553	0·302 −0·316	−0·634 −0·091
$M_y^{(2)}$	−0·096 −0·920	−0·061 −0·006	−0·209 0·020

† The characteristic dimension a is the length of the semi-major axis.

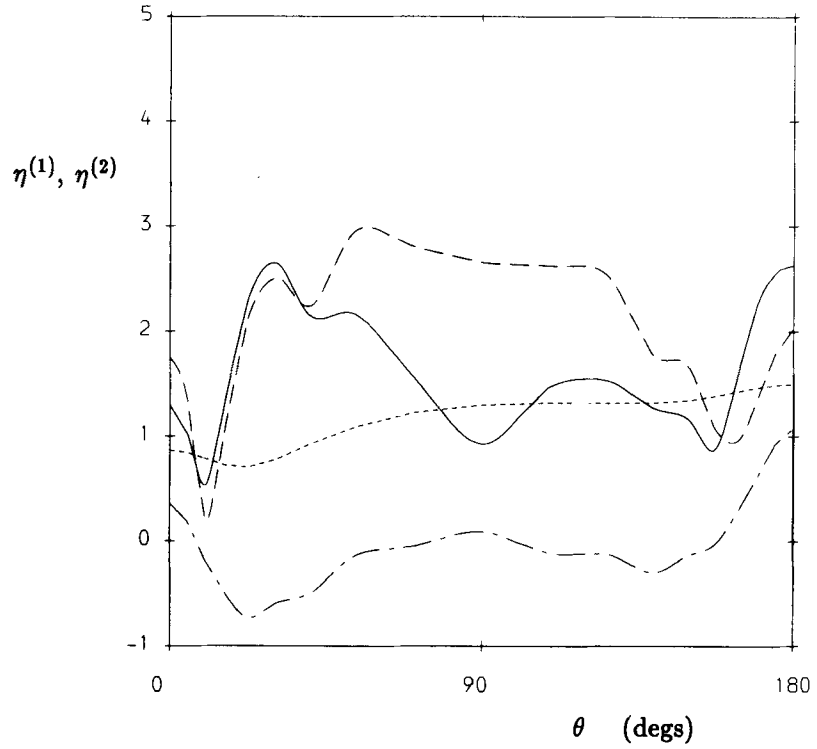

Figure 9. Modulus of the free surface elevation around an elliptic cylinder $b/a = 0{\cdot}5$, $d/a = 1{\cdot}0$, $ka = 2{\cdot}0$. FE mesh $10 \times 9 \times 8$ quadratic serendipity elements, $r_\infty/a = 2 + 2\pi$. First order elevation $|\eta^{(1)}|$: (------). Second order elevation $|\eta^{(2)}|$: (– – –). Second order elevation due to $\phi^{(2)}$, $|\eta_2^{(2)}|$: (———). Wave set-down $\bar{\eta}^{(2)}$: (— — —)

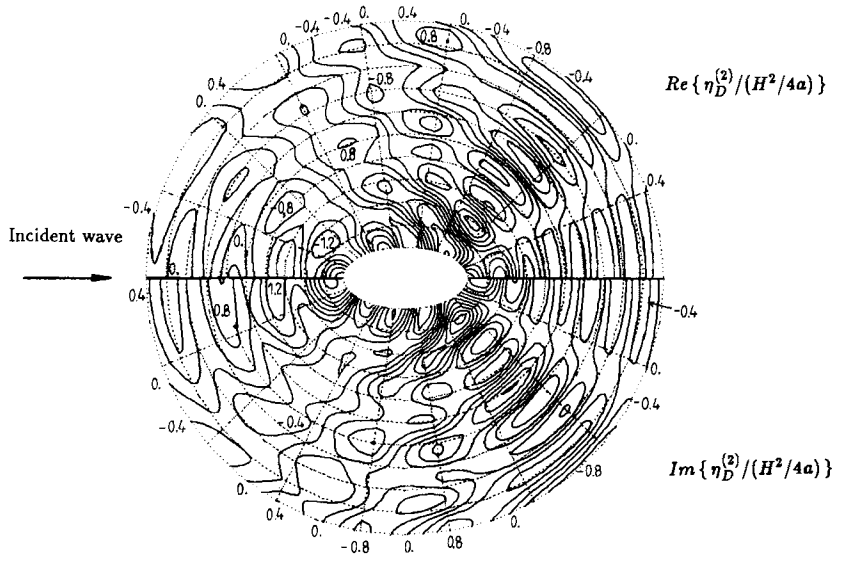

Figure 10. Contour plot of the free surface elevation due to $\phi_D^{(2)}$ around elliptic cylinder $b/a = 0{\cdot}5$, $d/a = 1{\cdot}0$, $ka = 2{\cdot}0$. The characteristic dimension a is the semi-major axis of the ellipse. FE mesh $10 \times 9 \times 8$ quadratic serendipity elements, $r_\infty/a = 2 + 2\pi$. The upper half is the real part, the lower half the imaginary part. The contours are drawn at intervals of 0·4

8. CONCLUSIONS

Methods for calculating non-linear wave loads on offshore structures using second-order Stokes wave theory are becoming well established nowadays. The 'indirect' methods of Lighthill[16] and Molin[15] for obtaining second-order forces have been verified by recently developed 'direct' methods.[22–26] The novel aspect of this paper is the application of the finite element method to the solution of the second-order boundary value problem. The results presented here have been compared with those of similar work based on Green's functions.[22–24] The original obstacle to the development of direct methods, i.e. a suitable radiation condition, has been overcome in this work by an adaption of the far-field equations for the locked wave diffraction potentials derived by Scolan[23,27] based on Molin's original analysis.[15] Kim and Yue[22] and Chau[24] have developed the radiation condition in a different form, yet there is a large measure of agreement between these different numerical procedures and the finite element results presented here. This greatly increases confidence in all these methods. Designers of offshore structures can have confidence in the application of non-linear diffraction theory as a result of these latest developments. Of particular concern to designers are the low-frequency resonant motions caused by non-linear wave excitation, and wave upwelling effects arising from multi-body interaction within compliant floating systems such as tension leg platforms. In addition, the finite element method is particularly suitable for extension to wave diffraction problems involving non-uniform water depths and stratified fluids.

ACKNOWLEDGEMENTS

The authors are indebted for the valuable discussions on second-order theory with Dr. B. Molin, Y. M. Scolan and X. Chen of the Institut Français du Petrole, with Prof. R. Eatock Taylor and F. P. Chau of University College London, and Prof. J. N. Hunt and Dr. D. Porter of the University of Reading. The financial support of the Marine Technology Directorate, Science and Engineering Research Council, through the award GR/E/2099.8 is gratefully acknowledged.

REFERENCES

1. T. H. Havelock, 'The pressure of water waves upon a fixed obstacle', *Proc. R. Soc. Lond. A*, **175**, 409–421 (1940).
2. C. J. Garrison, 'Hydrodynamic loading of large offshore structures', in O. C. Zienkiewicz *et al.* (eds), *Numerical Methods in Offshore Engineering*, Wiley, Chichester, 1978, pp. 87–140.
3. R. Eatock Taylor, 'Analysis of hydrodynamic loads by boundary element methods', in P. K. Banerjee and R. P. Shaw (eds), *Developments in Boundary Elements—2*, Applied Science Publishers, 1982.
4. O. C. Zienkiewicz, P. Bettess and D. W. Kelly, 'The finite element method for determining fluid loading on rigid structures', in O. C. Zienkiewicz *et al.* (eds), *Numerical Methods in Offshore Engineering*, Wiley, Chichester, 1978, pp. 141–183.
5. D. K. P. Yue, H. S. Chen and C. C. Mei, 'A hybrid element method for diffraction of water waves by three-dimensional bodies', *Int. j. numer. methods eng.*, **12**, 245–266 (1978).
6. C. C. Mei, *The Applied Dynamics of Ocean Surface Waves*, Wiley–Interscience, New York, 1983.
7. R. W. Yeung, 'Numerical methods in free surface flows', *Ann. Rev. Fluid Mech.*, **14**, 395–442 (1982).
8. N. Hogben, B. L. Miller, J. W. Searle and G. Ward, 'Estimation of fluid loading on offshore structures', *Proc. Inst. Civil Eng., Part 2*, **63**, 515–562 (1977).
9. S. K. Chakrabarti, *Hydrodynamics of Offshore Structures*, Computational Mechanics Publications, Southampton, 1987.
10. S. K. Chakrabarti, 'Comments on second-order wave effects on large-diameter vertical cylinder', *J. Ship Res.*, **22**, 266–268 (1978).
11. G. R. Mogridge and W. W. Jamieson, 'Wave loads on large circular cylinders: a design method', *National Research Council of Canada, Report No. MH-111*, Hydraulics Lab., Ottawa, 1976.
12. G. R. Mogridge and W. W. Jamieson, 'A design method for the estimation of wave loads on square caissons', *National Research Council of Canada, Report No. LTR-HY-57*, Hydraulics Lab., Ottawa, 1976.
13. A. Jeffrey and T. Kawahara, *Asymptotic Methods in Nonlinear Wave Theory*, Pitman, Boston, MA, 1982.

14. M. St. Q. Isaacson, 'Nonlinear wave forces on large offshore structures', *ASCE Trans. J. Waterway, Port, Coastal and Ocean Engineering*, **103**, 166–170 (1977).
15. B. Molin, 'Second order diffraction loads upon three-dimensional bodies', *Appl. Ocean Res.*, **1**, 197–202 (1979).
16. M. J. Lighthill, 'Waves and hydrodynamic loading', *Proc. 2nd Int. Conf. on the Behaviour of Offshore Structures, BOSS '79*, London, BURA Fluid Engineering, Cranfield, 1979, pp. 1–40.
17. B. Molin and A. Marion, 'Second-order loads and motions for floating bodies in regular waves', *Proc. 5th Int. Offshore Mechanics and Arctic Engineering Symp.*, Tokyo, American Society of Mechanical Engineers, New York, 1986, pp. 353–360.
18. R. Eatock Taylor and S. M. Hung, 'Second order diffraction forces on a vertical cylinder in regular waves', *Appl. Ocean Res.*, **9**, 19–30 (1987).
19. J. R. Hunt and R. E. Baddour, 'The diffraction of nonlinear progressive waves by a vertical cylinder', *Q. J. Mech. Appl. Math.*, **34**, 69–87 (1981).
20. P. F. Wang, 'The radiation condition and numerical aspects of second-order surface wave radiation and diffraction', *Ph.D. Thesis*, MIT, 1987.
21. K. Kurata and T. Ijima, 'Finite element analysis of wave forces on structures', *Proc. Civil Engineering in the Oceans/IV*, ASCE, San Fransisco, CA, 1979, pp. 172–186.
22. M. H. Kim and D. K. P. Yue, 'The complete second-order diffraction waves around an axisymmetric body, Part I, Monochromatic waves', *J. Fluid Mech.*, **200**, 235–264 (1989).
23. Y. M. Scolan and B. Molin, 'Second order deformation of the free-surface around a vertical cylinder', *4th Int. Workshop on Water Waves and Floating Bodies*, Norway, 1989.
24. F. P. Chau, 'The second order velocity potential for diffraction of waves by fixed offshore structures', *Ph.D. Thesis*, University College London, 1989.
25. P. J. Clark and P. Bettess, 'Experience solving second order diffraction problems using the finite element method', Department of Marine Technology Report, Newcastle upon Tyne University, 1990.
26. P. J. Clark, P. Bettess, G. E. Hearn and M. H. Downie, 'Second order wave diffraction by the finite element method', *Department of Marine Technology Report*, Newcastle upon Tyne University, February 1990.
27. Y. M. Scolan, Private communication, 1989.
28. K. Bando, P. Bettess and C. Emson, 'The effectiveness of dampers for the analysis of exterior scalar wave diffraction by cylinders and ellipsoids', *Int. j. numer. methods fluids*, **4**, 599–617 (1984).
29. O. C. Zienkiewicz, *The Finite Element Method*, 3rd edn, McGraw-Hill, London, 1977.
30. L. Boudet and Y. M. Scolan, 'Diffraction du second ordre sur un cylindre vertical: resultats numeriques et experimentaux', 2ième Journees de l'Hydrodynamique, Nantes, 1989.
31. N. Hogben, J. Osbourne and R. G. Standing, 'Wave loading on offshore structures—theory and experiment', *Symp. on Ocean Engineering*, RINA, London, 1975, pp. 19–36.
32. S. M. Hung, 'Second order wave forces on bodies in regular and bichromatic seas', *Ph.D. Thesis*, University College London, 1988.